https://doi.org/10.5194/egusphere-2026-1219
Preprint. Discussion started: 2 June 2026

Performance and methodological evaluation of a quantum-cascade-laser photoacoustic aerodynamic gradient system for field-scale NH_3 flux measurements

János Fekete[1], *Zoltán Bozóki*[1,3], *Csilla Gombi*[1], *László Horváth*[3*], *Zoltán Nagy*[2], *Krisztina Pintér*[2], *Tamás Weidinger*[4,5], *Anna Szabó*[1,3], *Helga Huszár*[1,3]

[1]Department of Optics and Quantum Electronics, Institute of Physics, University of Szeged, H-6720 Szeged, Hungary
[2]Department of Plant Physiology and Plant Ecology, Institute of Agronomy, Hungarian University for Agriculture and Life Sciences, H-2100 Gödöllő, Hungary
[3]HUN-REN-SZTE Research Group for Photoacoustic Monitoring of Environmental Processes, University of Szeged, H-6720 Szeged, Hungary
[4]Department of Meteorology, Institute of Geography and Earth Sciences, Eötvös Loránd University, H-1117 Budapest, Hungary
[5]Institute of Ecology and Botany, HUN-REN Centre for Ecological Research, H-2163 Vácrátót, Hungary

*corresponding author's e-mail: horvathl@titan.physx.u-szeged.hu

Abstract.
Reliable quantification of ammonia (NH_3) surface–atmosphere exchange remains challenging due to the compound's reactivity, inlet interactions, and the sensitivity of gradient-based flux estimates to instrumental response characteristics. We present the field evaluation and methodological assessment of a quantum-cascade-laser (QCL) based photoacoustic (PA) aerodynamic gradient system for half-hourly NH_3 flux measurements under agricultural conditions. The campaign covered a 54-day post-fertilization period under predominantly dry soil conditions, including the transition from bare soil to a developing winter rapeseed canopy. Instrumental performance was assessed through co-located inlet comparison experiments, yielding a random uncertainty of ±2 ppb (1σ) and demonstrating negligible systematic bias between sampling channels. The system operated continuously under field conditions with active thermal stabilization and humidity management. Fluxes were calculated using Monin-Obukhov similarity theory (MOST) across an ensemble of universal stability functions to evaluate methodological sensitivity. Sensitivity analysis indicated that variability attributable solely to stability-function selection remained small relative to observed diurnal flux amplitudes. Mean NH_3 emission during the investigated period was 1.85 nmol m^{-2} s^{-1}, corresponding to 1.21 kg N ha^{-1} or 4.0% of the applied fertilizer nitrogen. A pronounced diurnal asymmetry was observed, with daytime emissions approximately one order of magnitude higher than nighttime values, reflecting strong coupling between turbulent exchange and radiation-driven surface processes. Complementary machine-learning analysis indicated that incorporating short-term temporal memory substantially improved the representation of NH_3 flux dynamics and revealed distinct daytime and nighttime exchange regimes. The combined QCL–photoacoustic gradient system demonstrated robust field performance and low instrumental bias, supporting its applicability for long-term field-scale studies of reactive trace gas exchange.

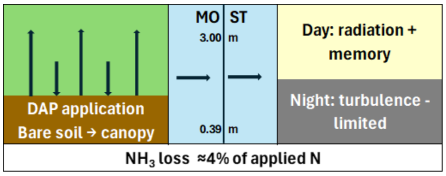

Key-words: Ammonia volatilization; Aerodynamic gradient method; Photoacoustic spectroscopy; Bidirectional NH_3 exchange; Monin-Obukhov similarity theory; Interpretable machine learning; Turbulent exchange

1. Introduction

The accumulation of reactive nitrogen (N_r) in the Earth system is a major environmental consequence of modern agriculture. Since the industrial fixation of atmospheric dinitrogen, large amounts of N_r have been introduced into ecosystems, where a single nitrogen atom may contribute sequentially to multiple impacts – air pollution, eutrophication, acidification, biodiversity loss and climate forcing – described as the nitrogen cascade (Galloway et al., 2003).

Ammonia (NH_3) is a central component of this cascade. It is the dominant alkaline gas in the atmosphere and a key precursor of secondary inorganic aerosol formation, thereby contributing to $PM_{2.5}$ burdens and associated health impacts (Seinfeld and Pandis, 2016). Deposition of NH_3/NH_4^+ also perturbs nutrient balances in sensitive ecosystems and can reduce plant species richness under elevated nitrogen inputs (Bobbink et al., 2010).

Agriculture accounts for the majority of global NH_3 emissions, with mineral fertilizer use being a major driver. Fertilizer-related NH_3 emissions have increased strongly since the 1960s and may further rise under future food demand and changing climate conditions (Sutton et al., 2013; Xu et al., 2019). From an agronomic perspective, NH_3 volatilization represents a direct loss of applied nitrogen and contributes to low nitrogen use efficiency at the global scale (e.g. Coskun et al., 2017; Bindraban et al., 2020).

Robust quantification of fertilizer-derived NH_3 losses is therefore essential both for environmental assessments and for evaluating mitigation options. However, NH_3 exchange measurements remain challenging because NH_3 is reactive and "sticky", shows strong interactions with wet surfaces, and commonly exhibits bidirectional exchange, with the surface acting as either a sink or a source depending on ambient concentrations and compensation point dynamics (Flechard et al., 2013). This complexity is amplified after fertilization, when soil emission potentials are high but canopy development increasingly promotes within-canopy uptake and recapture processes.

Micrometeorological flux methods (e.g., aerodynamic gradient, relaxed eddy accumulation, eddy covariance) are suitable for field-scale quantification, but they require accurate, fast-response concentration measurements. The performance of NH_3 instrumentation under field conditions has therefore been a long-standing focus, including large intercomparison efforts (von Bobrutzki et al., 2010). Besides chemical ionization mass spectrometry approaches enabling fast EC-type measurements (Sintermann et al., 2011), photoacoustic (PA) techniques have also been used in NH_3 monitoring and gradient applications (Pogány et al., 2010; Nelson et al., 2019; Kamp et al., 2020).

Photoacoustic approaches are attractive for long-term field deployment because of their sensitivity and continuous operation, but they are prone to practical issues relevant for gradient flux work: (i) humidity-related interferences, (ii) adsorption/desorption in sampling lines, and (iii) inlet switching and time-lag effects that can distort gradients if not handled carefully. Response-time and delay characteristics of PA multi-gas monitors have been explicitly investigated (Rom and Zhang, 2010), and diode-laser-based photoacoustic instruments have been developed and evaluated specifically for surface–atmosphere NH_3 flux applications (Pogány et al., 2010).

The primary objective of this study was to evaluate the field performance and methodological robustness of a QCL-based photoacoustic aerodynamic gradient system for

NH_3 flux measurements under agricultural conditions. NH_3 losses following mineral fertilizer application were quantified using aerodynamic gradient flux measurements combined with photoacoustic NH_3 mixing ratio observations. By covering the transition from bare soil shortly after fertilization to a developing crop canopy later in the season, the study targets a critical period when emission strengths and recapture processes change rapidly. Particular emphasis was placed on instrumental performance, methodological aspects of gradient-based flux calculations, and the robustness of Monin-Obukhov similarity-based flux estimates under field conditions. In addition, machine-learning analysis was applied as a complementary interpretative tool to investigate temporal dynamics and regime-dependent controls of the measured NH_3 fluxes.

2. Materials and Methods

2.1. Study Site and Experimental Conditions

Field measurements were carried out on an arable plot located near Kartal, Hungary, at the Gödöllő Experimental Farm. The observation period covered the late summer to early autumn growing season, extending from 28 August to 21 October 2025. The geographic coordinates of the site are 47° 39′ 42.56″ N, 19° 31′ 43.21″ E, with an elevation of approximately 153 m above sea level.

The region is characterized by a continental climate, with a long-term (1991–2020) mean annual precipitation of 550–600 mm. During the measurement campaign, cumulative precipitation amounted to 65 mm, resulting in predominantly dry soil conditions.

The soil at the site is classified as a Haplic Phaeozem (Humic, Pantoloamic) according to the World Reference Base for Soil Resources. Particle size analysis indicated a composition of 32.3% clay, 49.1% silt, and 18.6% sand, corresponding to a silty clay loam texture under the USDA classification scheme.

Field management prior to and during the experiment included mineral fertilization and crop establishment. On 25 August, the field was fertilized with 200 kg ha^{-1} of granular diammonium phosphate, equivalent to 30 kg N ha^{-1} and 80 kg P ha^{-1}. Winter rapeseed (*Brassica napus* L.) was sown two days later, on 27 August. As a result, the measurement period encompassed a transition from bare soil conditions immediately after fertilization to a developing crop canopy by mid-October.

2.2. Measurement Techniques and Instrumentation

2.2.1. Ammonia mixing ratio measurements

Ammonia mixing ratios were determined using a photoacoustic spectroscopy analyzer developed at the University of Szeged. One of the main components of the instrument is the data acquisition and control unit, which is a highly integrated embedded system developed by Videoton Holding Zrt. specifically for photoacoustic measurement systems.

The photoacoustic cell, thermostated at 50 °C separates the internal volume of the instrument from the sample gas flow. Acoustic signal generation takes place in one of the two resonators machined into the cell. This configuration is referred to as a differential photoacoustic cell (Miklós et al., 2001).

https://doi.org/10.5194/egusphere-2026-1219
Preprint. Discussion started: 2 June 2026

Acoustic signal detection is performed using two MEMS microphones (SisonicTM SPU0410HR5H-PB, Knowles). The microphones are connected to a differential amplifier, which performs signal preamplification, filtering, and analogue-to-digital conversion using a 16-bit ADC. Lock-in detection is implemented digitally; the Fourier transformation is carried out by an FPGA. The sampling rate is 50 kHz, resulting in a frequency resolution of approximately 12 Hz.

A quantum cascade laser (QCL) operating at a wavelength of 10.39 µm was used. This wavelength is suitable for ambient ammonia measurements, as ammonia is one of the dominant atmospheric absorbers at this wavelength under typical ambient conditions, minimizing spectral interference effects. In photoacoustic measurements, VOCs may cause a positive bias in the 10.39 µm (≈ 962 cm^{-1}) region due to spectral overlap (Liu et al., 2020); however, in our case, the use of a narrow-linewidth, small-bandwidth QCL allows targeting a specific, isolated absorption line, thereby effectively eliminating this interference. The optical output power of the QCL laser (model: QD10500CM1, Thorlabs) is approximately 50 mW. A mirror was placed at the end of the photoacoustic cell to double the effective optical path length and thereby enhance signal generation. Laser driving and temperature control were provided by a Thorlabs ITC4002QCL unit, while the modulation signal was generated by the control electronics of the instrument.

Air was sampled at two vertical levels, positioned at 0.39 m and 3.00 m above the soil surface, to enable flux estimation using the aerodynamic gradient method. Each measurement point consisted of 1 minute of flushing, followed by 2 minutes of data acquisition, repeated for each sampling level. Level selection was achieved using two solenoid valves (Asco SCH284B015). The sampling system was primarily constructed from PTFE tubing with an outer diameter of 6 mm and an inner diameter of 4 mm. The photoacoustic cell itself is made of stainless steel and was coated with a sodium hydroxide (1.5 M) solution to reduce ammonia adsorption. The volumetric flow rate was set to 800 cm^3 min^{-1}. A flow meter, a solenoid valve, and a needle valve were installed between the pump and the cell to ensure a stable and constant flow rate.

The sensitivity of the instrument was 17.9 µV ppb^{-1}, and the minimum detectable mixing ratio (DL) was approximately 3 ppb with 2 minutes of signal averaging, determined from the standard deviation (SD) and the slope of the calibration line as $DL = 3 \times SD / b$ (Shrivastava and Gupta, 2011). Approximately 97.5% of the measured values fell within the range 3–87 ppb, with a mean value of 20 ppb.

The complete system was installed in a standard electrical enclosure with additional thermal insulation. The enclosure has an IP66 rating, allowing operation under various outdoor weather conditions. The internal temperature of the enclosure was actively controlled and set to 42 °C. During periods of high ambient temperature, a protective tent was installed above the instrument to shield it from direct solar radiation and prevent overheating.

Prior to the field deployment, both inlet lines were temporarily placed at the same height to assess instrumental and sampling-related measurement uncertainty. For the flux calculations, mixing ratios (ppb) were converted to concentrations (nmol m^{-3}) using the molar volume at the given temperature and pressure.

To minimize gradient attenuation due to inlet adsorption–desorption effects, identical tubing materials and lengths were applied for both sampling heights, and inlet switching was preceded by a dedicated flushing period. Under steady-state conditions, the effective equilibration time of the system was shorter than the 2 min averaging interval, thereby limiting gradient distortion during half-hourly flux calculations.

2.2.2. Auxiliary meteorological and surface measurements

A comprehensive set of ancillary measurements was conducted to support flux calculations and interpretation. Three-dimensional wind speed and turbulence parameters were measured at 10 Hz using a METEK USA-1 ultrasonic anemometer. Soil physical conditions were monitored with a Campbell Scientific CS650 reflectometer, providing soil temperature and volumetric water content, from which water-filled pore space (WFPS) was derived. Air temperature and relative humidity were measured with a CS215 probe; precipitation was recorded using an ARG100 tipping bucket rain gauge; photosynthetically active radiation (*PAR*) was measured with an SKP215 quantum sensor; and global radiation (*I*g) was measured with a CM3 pyranometer. Crop development was characterized by repeated canopy transmittance measurements at seven permanent field locations using an AccuPAR LP-80 ceptometer, from which leaf area index (LAI) was derived. Leaf surface wetness was monitored with a PHYTOS-31 sensor. All instruments were connected to and synchronized by a Campbell Scientific CR3000 data logger, ensuring consistent time alignment across measurement systems.

High-frequency wind and scalar data from the sonic anemometer and a LiCor 7500 open-path infrared gas analyzer were processed using EddyPro software (version 7.0.9). Wind velocity, wind direction, friction velocity (u^*), temperature scale parameter (T^*), momentum flux, sensible and latent heat fluxes, and the Monin–Obukhov length were calculated from the 10 Hz measurements.

2.3. Flux Calculations

The turbulent ammonia flux was calculated using the aerodynamic gradient method with a 30-min averaging time interval at two measurement heights (z_1 = 0.39 m, z_2 = 3.00 m). During the calculations, the displacement height (d) was assumed to be 0.05 m. The friction velocity (u^*) and the Monin-Obukhov length (L) were measured and/or derived using an eddy-covariance measurement system. Flux calculations were based on Monin-Obukhov similarity theory (MOST) using a range of universal similarity functions reported in the literature; additionally, turbulent fluxes were also determined using the simplest logarithmic profile approximation.

A widely used approach for flux calculations based on trace gas gradient measurements is the application of universal stability functions that depend on atmospheric stability. Since NH_3 can generally be treated as a passive scalar in the surface layer, universal similarity functions developed for sensible heat transfer are commonly applied in aerodynamic gradient studies. This methodology has been used, among others, by Phillips et al. (2004); Spirig et al. (2010); Toyota et al. (2016); Kułek and Weidinger (2023); Zahn et al. (2023); and Abdulwahab et al. (2025), and is also described in methodological overviews of modern micrometeorological measurement techniques (Trebs et al., 2021).

In the case of stable stratification, 30 universal functions were applied together with logarithmic profiles characterized by two different Prandtl numbers (Tables A1 and A3), whereas under unstable stratification 22 universal functions were used together with two logarithmic profile formulations (Tables A2 and A3). These were selected based on the

https://doi.org/10.5194/egusphere-2026-1219
Preprint. Discussion started: 2 June 2026

synthesis studies of Högström (1988), Weidinger et al. (2000), Prueger and Kustas (2005), Kramm and Herbert (2009), Foken (2017), and a case study by Kułek and Weidinger (2023), as well as studies addressing turbulent exchange processes of trace gases. In addition to the classical logarithmic profile assumption (Prandtl number Pr = 1), several universal functions widely used in the literature were applied, such as those proposed by Businger et al. (1971) and Dyer (1974), later reformulated by Högström (1988).

The concentration gradient (Eq. 1) was expressed based on Monin-Obukhov similarity theory, adopting the commonly used assumption that the universal function describing trace gas transport has the same functional form as that for sensible heat transport $\varphi_c(\zeta) \equiv \varphi_H(\zeta)$ (Mayer et al., 2011; Zahn et al., 2023; Abdulwahab et al., 2025). The profile equation for concentration gradient is

$$\frac{\partial \bar{c}}{\partial \ln(z-d)} \cong \frac{\Delta \bar{c}}{\Delta \ln(z-d)} = \frac{\bar{c}_2-\bar{c}_1}{\ln(z_2-d)-\ln(z_1-d)} = \frac{c_*}{\kappa}\varphi_c(\zeta_k), \qquad (1)$$

where c_* is the dynamical concentration scale for the NH_3 flux calculation, $\bar{c}_1$ and $\bar{c}_2$ are the 30-min mean concentrations.

Assuming a near-logarithmic profile, the dimensionless height was defined as $\zeta_k = z_k/L$, where z_k denotes the geometric mean height of the two measurement levels:

$$z_k = \sqrt{(z_1-d)(z_2-d)}. \qquad (2)$$

Although the integral form of Eq. (1) could also be applied (Weidinger et al., 2000; Foken, 2017; Foken and Mauder, 2024), for two closely spaced measurement levels the direct calculation using Eq. (1) provides sufficiently accurate results (Arya, 1991). Comparative calculations were performed using the two most commonly applied universal functions (Businger et al., 1971; Dyer, 1974), revealing negligible differences between the two approaches.

Universal functions have generally been validated within the interval $-1 \leq \zeta \leq +1$. In extremely stable ($\zeta > 1$) or extremely unstable ($\zeta < -1$) conditions – representing approximately 2% of the cases – the critical dimensionless heights ($\zeta_{krit} = 1$, if $\zeta > 1$, $\zeta_{krit} = -1$, if $\zeta < -1$) was applied in the calculations, while retaining the original stability classification.

The i-th type of dynamical concentration scale, c_{*i} was calculated based on the corresponding universal function, $\varphi_{ci}(\zeta_k)$ and von Karman-constant, κ_i from equation (1):

$$c_{*i} \cong \frac{\kappa_i}{\varphi_{ci}(\zeta_k)} \frac{\bar{c}_2-\bar{c}_1}{\ln(z_2-d)-\ln(z_1-d)}. \qquad (3)$$

The 30-min ammonia flux was obtained by averaging the individual flux estimates:

$$F_{NH_3} = \frac{1}{N}\sum_{i=1}^{N}(-u_* c_{*i}), \qquad (4)$$

where $N = 30$ for stable or neutral stratification ($\zeta_k \geq 0$) and $N = 22$ for unstable ($\zeta_k < 0$) stratification, including the two logarithmic profile approaches in both cases (Tables A1–A3).

To evaluate methodological robustness, fluxes were calculated using a comprehensive ensemble of universal similarity functions under both stable and unstable stratification.

Sensitivity analysis showed that the variability attributable solely to stability-function selection remained small relative to observed diurnal flux amplitudes, indicating that the dominant uncertainty did not arise from similarity-function choice.

2.4. Machine Learning Analysis

Because ammonia flux time series inherently exhibit strong autocorrelation and non-stationarity, strict chronological validation was implemented to prevent temporal leakage. This design ensures that predictive performance reflects genuine forward extrapolation in time rather than artefacts arising from random data partitioning.

Half-hourly NH_3 fluxes (nmol m^{-2} s^{-1}) were analyzed over a multi-day post-fertilization period (n = 2590 observations). The dataset included a comprehensive set of candidate predictors encompassing structural variables (leaf area index), soil physical properties (volumetric water content, water-filled pore space, soil temperature), meteorological drivers (air temperature, relative humidity, precipitation, global radiation, photosynthetically active radiation), turbulent exchange parameters (friction velocity, momentum flux, sensible and latent heat fluxes, wind speed and direction, Monin-Obukhov length), chemical variables (NH_3 concentration at 3 m), management-related variables (days after fertilization), and derived aerodynamic and boundary layer resistances. All predictors were initially included in the model without subjective pre-selection.

The flux time series exhibited three dominant structural characteristics: a pronounced diurnal cycle with nighttime minima and daytime maxima, a progressive decay following fertilizer application, and strong short-term autocorrelation at sub-daily scale. Because these properties violate assumptions of independence and stationarity, a time-aware modelling framework was adopted.

To prevent temporal leakage, model validation was conducted using a strictly chronological split. The first 80% of days were used for training and the remaining 20% were reserved as an independent test set representing forward prediction in time. No random cross-validation was applied.

Model performance was evaluated exclusively on the final 20% of days, chronologically withheld from model training to represent forward prediction in time, using the coefficient of determination (R^2), root mean square error (RMSE) and mean absolute error (MAE).

To account for short-term dynamical persistence, autoregressive lag features were introduced to represent intrinsic system memory. Specifically, NH_3 flux values from the previous six half-hour intervals (NH_{3t-1} to NH_{3t-6}), corresponding to a three-hour memory window, were included as predictors. Lagged values crossing day boundaries were masked to avoid artificial carryover effects.

An Extremely Randomized Trees (ExtraTrees) regression model was employed due to its ability to capture nonlinear relationships, resolve high-order interactions, and remain robust in the presence of correlated predictors without assuming linearity. Missing values were handled using median imputation fitted on the training dataset and applied consistently to the test data.

To interpret model structure and underlying mechanisms, three complementary approaches were applied: impurity-based and permutation feature importance to identify dominant predictors, Partial Dependence (PDP) and Individual Conditional Expectation

(ICE) curves to visualize nonlinear responses, and Friedman's H-statistic to quantify the strength of pairwise nonlinear interactions. Residual autocorrelation within days was additionally evaluated using autocorrelation functions (ACF) to assess remaining temporal structure after modelling. Finally, regime-specific analyses were performed separately for daytime ($PAR > 0$) and nighttime ($PAR = 0$) conditions to identify potential shifts in dominant environmental controls.

3. Results and discussion

3.1. Uncertainty Estimation and Measurement Reliability

To assess the measurement reliability and random uncertainty of the system, samples were collected at a single inlet height, applying two-minute temporal averaging. This averaging strategy suppresses short-term fluctuations and ensures that the comparison predominantly reflects instrumental and sampling uncertainties, rather than environmental variability.

During the comparison period, both sampling channels operated at an identical height of 300 cm. Under these conditions, the agreement between the two datasets was excellent. The Pearson correlation coefficient ($r = 0.97$) indicates a strong linear relationship. Linear regression yielded $a = 0.97 \times b + 0.60$, demonstrating an almost one-to-one correspondence with only a minor offset.

The mean difference between the two channels was +0.28 ppb, and the standard deviation of the differences was 2.06 ppb. The absence of a significant systematic bias suggests that the observed deviations are dominated by instrumental noise and sampling uncertainty.

Based on these results, the typical random measurement uncertainty between the two channels under identical sampling conditions is estimated to be ±2 ppb (1σ). Accordingly, the upper bound of the random error at the 95% confidence level ($\pm 1.96\ \sigma$) is approximately ±4 ppb.

3.2. Diurnal Variation of Ammonia Flux and Turbulent Exchange

Ammonia fluxes during nighttime were relatively stable, ranging between −0.08 and 0.72 nmol $m^{-2}\ s^{-1}$. In contrast, the daytime period exhibited a pronounced diurnal pattern characterized by a distinct maximum in the late morning hours. This behavior can be attributed primarily to the diurnal dynamics of turbulent exchange.

Ammonia fluxes were calculated using Monin-Obukhov similarity theory (MOST) based on vertical concentration gradients and micrometeorological parameters. For diagnostic purposes, an effective turbulent transfer coefficient (K_c) was derived such that

$$F = K_c\left(\frac{\Delta C}{\Delta z}\right), \tag{5}$$

where K_c represents the stability-corrected exchange coefficient obtained from the MOST framework rather than an independently fitted parameter.

The turbulent diffusion coefficient (K_c), calculated from two-minute averaged flux and concentration gradient data demonstrated a clear diurnal course. During the nighttime period (4:00 p.m.-03:00 a.m., UTC, zonal time is UTC+2), K_c averaged 0.06 $m^2\ s^{-1}$, indicating suppressed turbulent mixing due to limited surface energy input. In contrast, daytime values increased substantially, reaching approximately 0.17 $m^2\ s^{-1}$ (Fig. 1), reflecting enhanced convective turbulence under higher radiation and thermal forcing.

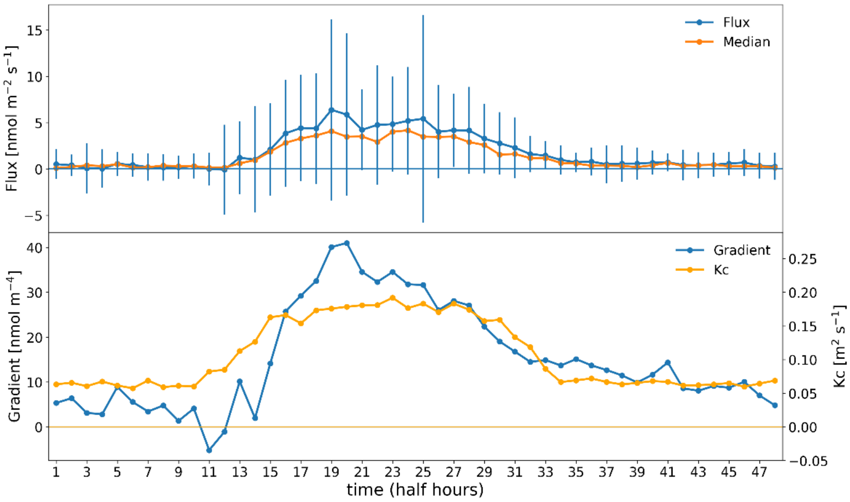

Figure 1. Upper panel: Diurnal cycle of NH_3 flux. Vertical bars indicate ±1 standard deviation (SD) of half-hourly flux values. Lower panel: half-hourly gradients and diffusion coefficients. The horizontal axis represents half-hourly time steps (1–48). Time is given in UTC; local standard time at the measurement site is UTC+2.

The concentration gradient exhibited a similar daytime maximum, and together with K_c, governed the diurnal evolution of ammonia flux. Fluxes peaked at approximately 09:00 (11:00 local time), followed by a local minimum around midday. This midday reduction may be consistent with commonly observed stomatal regulation phenomena.

Ammonia emission via plant stomata appears to be partially constrained during midday hours. Elevated temperature and high vapor pressure deficit increase transpiration demand, leading to transient plant water stress. In response, plants regulate stomatal aperture through abscisic acid (ABA)-mediated signaling, resulting in partial stomatal closure even under high irradiance conditions. Midday stomatal closure is primarily driven by high vapor pressure deficit and plant water stress (Oren et al., 1999), and stomatal regulation functions as an active, ABA-mediated control of photosynthesis (Flexas and Medrano, 2002).

Despite reduced turbulent exchange during nighttime, the concentration gradient remained small. This suggests that nocturnal ammonia emissions were limited, resulting in near-equilibrium conditions between the surface and the overlying air layer. Under such conditions, reduced mixing does not necessarily lead to concentration build-up, as the source strength is insufficient to generate a pronounced vertical gradient (Sutton et al., 1995; Nemitz et al., 2000).

In our study, as shown in Figure 1, emission dominates during the daytime hours, with a maximum around noon, whereas during the nighttime it shows relatively constant, low values and occasionally shifts to deposition. When separated based on global radiation and photosynthetically active radiation, the mean emission was 3.11 nmol $m^{-2}\ s^{-1}$ under $I_g > 0$ and $PAR > 0$ conditions, while during nighttime hours ($I_g = PAR = 0$) it was an order of magnitude lower, 0.448 nmol $m^{-2}\ s^{-1}$.

The daytime dominance of ammonia flux has long been recognized. For example, Harper et al. (1983) reported that the daily NH_3 cycle was pronounced, with substantial emission during the day and small emissions or even deposition at night. During the summer season, soil surface temperature was the factor most strongly correlated with NH_3 flux. During the remainder of the year, evapotranspiration showed the highest correlation, although the increased midday flux was likely attributable to the parallel increase in soil temperature and wind speed. All of the main influencing factors are interrelated through their dependence on solar radiation.

In a review study, Hargrove (1988) listed several factors determining ammonia flux. Environmental variables such as temperature, soil moisture content, and air exchange at the soil surface are primary determinants of the magnitude of NH_3 loss. Soil moisture and surface air exchange are particularly important. Under field conditions, these factors fluctuate widely on a daily basis due to the combined effects of dew formation and evaporation. Studies cited in Hargrove (1988) indicate that, on a daily scale, high NH_3 loss rates are generally associated with periods of rapid soil drying, when moist (near field capacity) surface soil is followed by several days with little or no rainfall (<0.5 inches). It is also evident that NH_3 loss is related to wind speed under field conditions, and that low air exchange rates at the soil surface—such as those expected within a plant canopy or in no-till production systems—may limit NH_3 loss.

Recent research has reinforced that ammonia emissions are strongly controlled by interactions among soil properties, meteorological conditions, and management practices. Advanced atmospheric emission models show that incorporating spatial and temporal variability in agricultural activities, such as manure and fertilizer application timing, as well as explicit representation of soil moisture and temperature, significantly improves simulation of observed NH_3 emission dynamics across Europe and beyond (Ge et al., 2020). Field and satellite-based studies further highlight that environmental drivers and atmospheric lifetime of NH_3 vary considerably with local conditions, affecting both emission rates and dispersion patterns (Xie et al., 2024). Reviews also emphasize the profound contribution of agriculture to global ammonia emissions and their impacts on particulate formation and human health, underscoring the need to account for complex environmental dependencies when estimating NH_3 fluxes (Wyer, 2022).

It is therefore clear that identifying the factors controlling emission is not straightforward, as their relative importance varies depending on the specific environmental conditions.

3.3. Temporal Variation of Ammonia Emission

During the investigated period (4.662×10^6 s), the mean ammonia emission was 1.85 nmol $m^{-2}\ s^{-1}$, corresponding to 1.21 kg ha^{-1} when expressed as nitrogen, representing 4.0% of the applied fertilizer nitrogen.

Emission dynamics were strongly time-dependent (Fig. 2). Immediately after fertilization, elevated fluxes were observed under bare soil conditions, reflecting high surface emission potential. In the following days, fluxes declined progressively, consistent with depletion of readily volatilizable ammonium and changes in soil-surface equilibrium conditions.

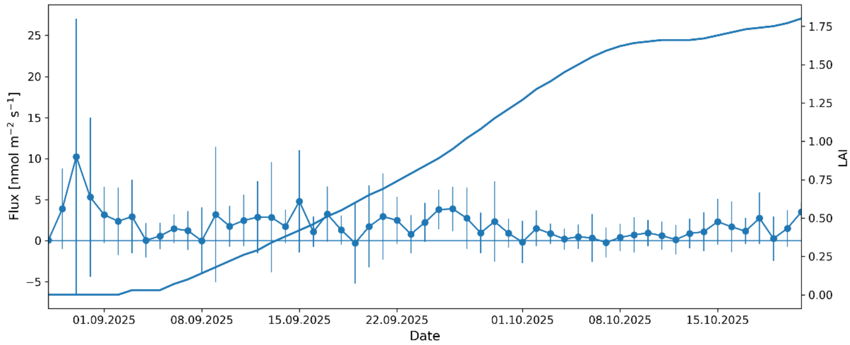

Figure 2. Temporal variation of NH_3 flux and increase of leaf area index (LAI). Vertical bars indicate ±1 standard deviation (SD) of half-hourly fluxes for each day.

Superimposed on this seasonal-scale decay, pronounced short-term variability was observed, driven by diurnal changes in radiation and turbulent exchange as discussed in Section 3.2. The overall fertilizer-related nitrogen loss (4%) falls within the lower range reported in the literature for similar mineral fertilizer applications under relatively dry soil conditions.

Synthetic nitrogen fertilizers are applied in various forms, including urea, ammonium nitrate, ammonium sulphate, calcium ammonium nitrate, UAN, and phosphate-based ammonium fertilizers (Amhamed et al., 2022). Following application, a portion of ammonium is taken up by plants or transformed through nitrification, while a significant fraction may be lost via gaseous emissions – particularly as NH_3, which typically peaks shortly after fertilization and can account for 6-20% of applied nitrogen depending on fertilizer type, soil properties, climate, and management practices (Génermont and Cellier, 1997; Sommer et al., 2004; Zhan et al., 2020; Ma et al., 2021). Emission responses are strongly nonlinear and often increase exponentially with application rate (Jiang et al., 2017). Huang et al. (2017) reported that under mineral fertilizer treatments (NK/NP/NPK), total NH_3 volatilization losses were ≤4.2% of the applied nitrogen, whereas substantially higher losses were observed under combined organic and mineral fertilization.

In the present study, di-ammonium phosphate (DAP) was applied at a moderate rate and compared to urea-based fertilizers its volatilization potential is generally lower; consequently, the expected NH_3 loss response is less pronounced even under nonlinear dose–response relationships.

3.4. Interpretable Machine Learning Analysis of NH_3 Flux Dynamics

To further interpret the temporal variability of the measured NH_3 fluxes, an exploratory machine-learning analysis was performed using the observational dataset. The half-hourly NH_3 flux time series exhibited a pronounced diurnal cycle, a progressive decay trend, and strong short-term autocorrelation. Therefore, model validation was conducted using a strictly chronological (day-aware) split, with the first 80% of days used for training and the remaining 20% reserved for forward evaluation.

Models based solely on contemporaneous meteorological predictors showed negligible predictive skill (R^2_test ≈ 0.01), indicating that instantaneous environmental drivers alone were insufficient to explain cross-day variability. Residual diagnostics revealed strong within-day persistence (lag –1 autocorrelation ≈ 0.33), motivating the explicit inclusion of autoregressive lag features up to six half-hour steps (3 hours). Incorporating this short-term memory structure markedly improved predictive performance (R^2_test ≈ 0.31) and reduced residual autocorrelation to near white-noise levels (lag-1 ACF ≈ 0.05). For the full dataset, inclusion of lag features increased predictive skill to R2_test ≈ 0.31. Subsequent regime-specific modelling further revealed distinct daytime and nighttime control structures.

Model interpretation revealed regime-dependent nonlinear controls. During daytime conditions (*PAR* > 0), radiation-related variables interacted strongly with autoregressive memory terms. ICE curves for NH3_lag_1 under daytime conditions (Figure 3) showed consistent positive persistence effects, while two-dimensional partial dependence surfaces (Figure 4) indicated that the influence of prior flux state was amplified under high *PAR*. This pattern suggests radiation-modulated volatilization from a dynamically buffered surface reservoir, where energy availability enhances release efficiency conditional on recent emission history.

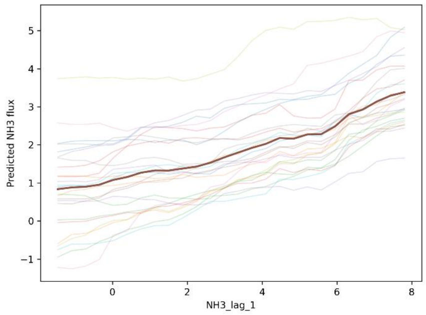

Figure 3. Individual Conditional Expectation (ICE) curves for NH_3_lag_1 under daytime conditions (*PAR* > 0). Thin lines represent individual conditional responses, while the thick line shows the mean partial dependence.

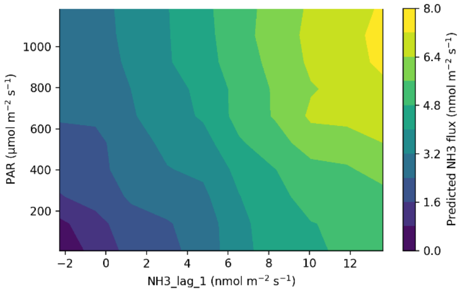

Figure 4. Partial dependence surface of predicted NH_3 flux as a function of NH_3 lag-1 and *PAR* under daytime conditions (*PAR* > 0). Colors indicate predicted NH_3 flux (nmol m^{-2} s^{-1}) using the full value range of the model-predicted values for the daytime subset.

In contrast, nighttime conditions (*PAR* = 0) displayed a fundamentally different control structure. Radiation lost explanatory power, and turbulent transport metrics such as friction velocity (*u**) and wind speed became dominant. ICE curves for *u** (Figure 5) revealed threshold-like behavior, with suppressed flux under weak turbulence and rapid increases once mixing intensified. Two-dimensional interaction surfaces (Figure 6) confirmed that nighttime flux is primarily transport-limited, with strong nonlinear coupling between turbulence intensity and wind speed. Autoregressive memory remained relevant but interacted with mixing conditions rather than radiative forcing.

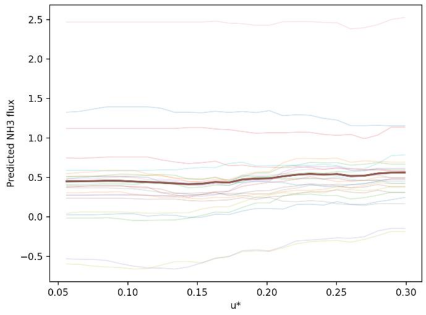

Figure 5. Individual Conditional Expectation (ICE) curves for friction velocity (u^*, m s^{-1}) under nighttime conditions ($PAR = 0$). Predicted NH_3 flux (nmol m^{-2} s^{-1}) shows threshold-like behavior, with suppressed emissions at low turbulence and rapid increases once mixing intensifies.

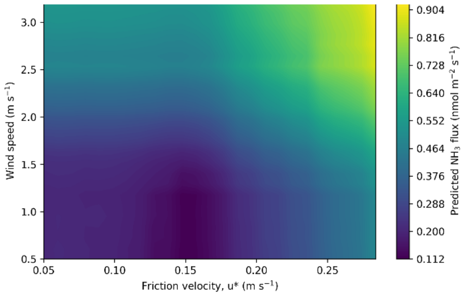

Figure 6. Partial dependence surface of predicted NH_3 flux as a function of friction velocity (u^*) and wind speed under nighttime conditions ($PAR = 0$). Colors indicate predicted NH_3 flux (nmol m^{-2} s^{-1}) using the full value range of the nighttime subset; the color scale is not shared with Figure 4.

Together, these results demonstrate a clear regime shift between daytime and nighttime NH_3 exchange. Daytime flux is characterized by radiation-amplified persistence, whereas nighttime flux is controlled by turbulence-limited release. The identified ~3-hour system memory and regime-dependent nonlinear interactions indicate that NH_3 emissions reflect a transient soil–surface reservoir modulated by environmental forcing rather than a purely instantaneous response. Chronological validation further highlights that ignoring temporal structure can substantially overestimate predictive skill. These analyses suggest that incorporating temporal persistence and regime-specific environmental controls may improve the interpretation of NH_3 flux dynamics.

Despite the inclusion of multiple soil, meteorological, and turbulence-related predictors, permutation importance consistently highlighted *PAR* and friction velocity (u^*) as dominant controls. The compensation point concentration of the soil-plant system was not directly measured. The inferred reservoir behavior is consistent with, but does not directly quantify, soil–plant compensation point dynamics. Finally, regime-specific analyses were performed separately for daytime ($PAR > 0$) and nighttime ($PAR = 0$) conditions to identify potential shifts in dominant environmental controls. Separate ExtraTrees models were fitted for the two subsets to resolve regime-specific controls.

4. Conclusions

This study presented the field evaluation and methodological assessment of a photoacoustic NH_3 measurement system combined with an aerodynamic gradient approach for quantifying bidirectional ammonia exchange following mineral fertilizer application under agricultural conditions. The measurement period covered the transition from bare soil to a developing winter rapeseed canopy, enabling the investigation of both emission intensity and evolving exchange dynamics under realistic field conditions.

The combined QCL-photoacoustic gradient system demonstrated robust and stable field performance during continuous long-term operation. Co-located inlet comparison experiments indicated low instrumental bias between sampling channels and a typical random uncertainty of approximately ±2 ppb (1σ). The implemented thermal stabilization, humidity management, and inlet-switching protocol proved suitable for minimizing gradient distortion and maintaining reliable operation under variable outdoor conditions.

Flux calculations based on Monin-Obukhov similarity theory (MOST) using a comprehensive ensemble of universal stability functions showed good methodological consistency. Sensitivity analysis demonstrated that variability attributable solely to stability-function selection remained small relative to the observed diurnal variability of NH_3 exchange, indicating that the dominant uncertainty did not arise from the choice of similarity function itself.

The cumulative NH_3 loss amounted to 1.21 kg N ha^{-1}, corresponding to 4.0% of the applied fertilizer nitrogen. A clear and quantitatively resolved diurnal asymmetry was observed, with mean daytime emissions ($Ig > 0$, $PAR > 0$) reaching 3.11 nmol m^{-2} s^{-1}, approximately one order of magnitude higher than nighttime values (0.448 nmol m^{-2} s^{-1}). This pronounced day–night contrast indicates that post-fertilization NH_3 exchange is strongly coupled to radiation-driven turbulent and surface processes during daytime, whereas nighttime exchange is primarily limited by turbulent transport conditions.

Complementary machine-learning analysis suggested that short-term temporal persistence plays an important role in NH_3 flux dynamics and revealed distinct daytime and nighttime exchange regimes. However, the primary outcome of the study is the demonstration that the presented QCL-based photoacoustic aerodynamic gradient system provides a reliable framework for long-term field-scale NH_3 flux measurements and methodological investigations of reactive trace gas exchange under agricultural conditions.

Author Contributions

ZB and LH designed the experiments.
JF, CG, HH, ZN, KP, and AS carried out the field measurements and contributed to data acquisition.
LH prepared the manuscript with contributions from all co-authors.
TW performed the flux calculations.

The datasets are available in the of University of Szeged repository:
https://doi.org/10.82570/SZTE_Datarepo_b7hfb-dms70

Acknowledgements

The authors gratefully acknowledge the Agro-Ecological Station at the Experimental Farm in Gödöllő for providing the opportunity to conduct measurements, as well as the staff responsible for its operation for their assistance. Generative AI tools were used for language editing and figure preparation support. All analyses, interpretations, and scientific conclusions were performed and verified by the authors.

Financial support

The research was funded by the Sustainable Development and Technologies National Programme of the Hungarian Academy of Sciences (FFT NP FTA), and by the Hungarian Research and Technology Innovation Fund (OTKA), project no. K-138176.

Declaration of Competing Interest

The authors declare that they have no conflict of interest.

References

Abdulwahab, M.O., Flechard, C., Fauvel, Y., Häni, C., Jacotot, A., Graux, A. I., Edouard, N., Buysse, P., Viaud, V. Neftel, A., 2025. Aerodynamic gradient flux measurements of ammonia in intensively grazed grassland: temporal variations, environmental drivers, methodological challenges and uncertainties. EGUsphere 2025, 1–46.

Amhamed, A.I., Shuibul Qarnain, S., Hewlett, S., Sodiq, A., Abdellatif, Y., Isaifan, R.J., Alrebei, O.F., 2022. Ammonia production plants – a review. Fuels, 3(3), 408–435.

Arya, P.S., 2001. Introduction to micrometeorology. International Geophysics Series 79, Academic Press, San Diego, San Francisco, New York, Boston, London, Sydney, Tokyo. Second edition.

Arya, S.P.S., Plate, E.J., 1969. Modeling of the Stable Stratified Atmospheric Boundary Layer. Journal of the Atmospheric Sciences 26, 656–665.

Badgley, F.I., Paulson, C.A., Miyake, M., 1972. Profiles of Wind, Temperature and Humidity over the Arabian Sea. The University Press of Hawaii, 62 pp. eBook ISBN: 9780824891251. https://doi.org/10.1515/9780824891251

Beljaars, A.C.M., Holtslag, A.A.M., 1991. Flux parametrization over land surfaces for atmospheric models. Journal of Applied Meteorology and Climatology 30(3), 327–341. https://doi.org/10.1175/1520-0450(1991)030<0327:FPOLSF>2.0.CO;2

Bindraban, P.S., Dimkpa, C.O., White, J.C., Franklin, F.A., Melse-Boonstra, A., Koele, N., et al., 2020. Safeguarding human and planetary health demands a fertilizer sector transformation. Plants People Planet 2, 302–309.

Bobbink, R., Hicks, K., Galloway, J., Spranger, T., Alkemade, R., Ashmore, M., et al., 2010. Global assessment of nitrogen deposition effects on terrestrial plant diversity: a synthesis. Ecological Applications, 20, 30–59.

Businger, J.A., Wyngaard, J.C., Izumi, Y., Bradley, E.F., 1971. Flux-profile relationships in the atmospheric surface layer. Journal of the Atmospheric Sciences, 28:181–189. https://doi.org/10.1175/1520-0469(1971)028<0181:FPRITA>2.0.CO;2

Carl, D.M., Tarbell, T.C., Panofsky, H.A., 1973. Profiles of Wind and Temperature from Towers over Homogeneous Terrain. Journal of the Atmospheric Sciences 30(5), 788–794. https://doi.org/10.1175/1520-0469(1973)030<0788:POWATF>2.0.CO;2

Chenge, Y., Brutsaert, W., 2005. Flux-profile Relationships for Wind Speed and Temperature in the Stable Atmospheric Boundary Layer. Boundary-Layer Meteorol **114**, 519–538. https://doi.org/10.1007/

Coskun, D., Britto, D.T., Shi, W., Kronzucker, H.J., 2017. Nitrogen transformations in modern agriculture and the role of biological nitrification inhibition. Nature Plants 3, 1–10.

Dyer, J., 1974. A review of flux-profile-relationships. Boundary-Layer Meteorology 7, 363–372. https://doi.org/10.1007/bf00240838

Dyer, A.J., Bradley, E. F., 1982. An Alternative Analysis of Flux-Gradient Relationships at the 1976 ITCE. Boundary-Layer Meteorology 22, 3–19. https://doi.org/10.1007/BF00128053

https://doi.org/10.5194/egusphere-2026-1219
Preprint. Discussion started: 2 June 2026

Dyer, A.J., Hicks, B.B., 1970. Flux-gradient relationships in the constant flux layer. Quarterly Journal of the Royal Meteorological Society 96:715–721. https://doi.org/10.1002/qj.49709641012

Edwards, G.C., Rasmussen, P.E., Schroeder, W.H., Wallace, D.M., Halfpenny-Mitchell, L., Dias, G.M., et al., 2005. Development and evaluation of a sampling system to determine gaseous Mercury fluxes using an aerodynamic micrometeorological gradient method. Journal of Geophysical Research: Atmospheres, 110, D10306. doi:10.1029/2004JD005187

Flechard, C.R., Fowler, D., Sutton, M.A., et al., 2013. Advances in understanding, models and parameterizations of biosphere-atmosphere ammonia exchange. Biogeosciences, 10, 5183–5220.

Flexas, J., Medrano, H., 2002. Drought‐inhibition of photosynthesis in C3 plants: stomatal and non‐stomatal limitations revisited. Annals of botany, 89(2), 183–189.

Foken T., Skeib G., 1983. Profile measurements in the atmospheric near-surface layer and the use of suitable universal functions for the determination of the turbulent energy exchange. Boundary-Layer Meteorology 25, 55–62. https://doi.org/10.1007/BF00122097

Foken, T., 2017. Micrometeorology. Springer International Publishing. ISBN 978-3-642-25440-6 (eBook). https://doi.org10.1007/978-3-642-25440-6

Foken, T., and Mauder, M., 2024. Micrometeorology. Atmospheric Science Series. Springer, Berlin. https://doi.org/10.1007/978-3-031-47526-9

Fukui, K., Nakajama, M., Ueda, H., 1983. A laboratory experiment on momentum and heat transfer in the stratified surface layer. Quarterly Journal of the Royal Meteorological Society l09, 661–676. https://doi.org/10.1002/qj.49710946114

Galloway, J.N., Aber, J.D., Erisman, J.W., Seitzinger, S.P., Howarth, R.W., Cowling, E B., & Cosby, B.J., 2003. The nitrogen cascade. BioScience, 53, 341–356.

Gavrilov, A S., Petrov, J.S., 1981. Ocenka totschnosti opredelenija turbulentnych potokov po standartnym gidrometeorologitscheskim izmerenijam nad morem. Meteorologia i Gidrologia 4, 52–59 (In Russian).

Ge, X., Schaap, M., Kranenburg, R., Segers, A., Reinds, G.J., Kros, H., de Vries, W., 2020. Modeling atmospheric ammonia using agricultural emissions with improved spatial variability and temporal dynamics. Atmospheric Chemistry and Physics 20, 16055–16087. https://doi.org/10.5194/acp-20-16055-2020

Génermont, S., Cellier P, 1997. A mechanistic model for estimating ammonia volatilization from slurry applied to bare soil. Agricultural and Forest Meteorology 88:145–167

Handorf, D., Foken, T., Kottmeier, C., 1999. The stable atmospheric boundary layer over an Antarctic ice sheet. Boundary-Layer Meteorology 91:165–186. https://doi.org/10.1023/A:1001889423449

Hargrove, W.L., 1988. Evaluation of ammonia volatilization in the field. Journal of production agriculture 1(2), 104–111.

Harper, L.A., Catchpoole, V.R., Davis, R., Weir, K L., 1983. Ammonia volatilization: soil, plant, and microclimate effects on diurnal and seasonal fluctuations 1. Agronomy Journal 75(2), 212–218.

Högström, U., 1988. Non-dimensional wind and temperature profiles in the atmospheric surface layer: A re-evaluation. Boundary-Layer Meteorology **42**, 55–78. https://doi.org/10.1007/

Huang, J., Zhang, X.B., Zhang, Y.Z., Sun, N., 2017. Nitrogen mobility, ammonia volatilization, and estimated leaching loss from long-term manure incorporation in red soil. Journal of integrative agriculture, 16(9), 2082–2092.

Hurtalova, T., Szabo, T., 1985. Abhängigkeit der Turbulenz-Charakteristiken von der Temperaturschichtung der Atmosphäre (The dependence of the turbulent characteristics of the thermal stratifiaction in the atmosphere). Zeitschrift für Meteorologie 35(6), 349–353 (In German).

Jiang, Y., Deng, A., Bloszies, S., Huang, S., Zhang, W., 2017. Nonlinear response of soil ammonia emissions to fertilizer nitrogen. Biology and Fertility of Soils 53, 269–274.

Kamp, J.N., Häni, C., Nyord, T., Feilberg, A., Sørensen, L.L., 2020. The aerodynamic gradient method: implications of non-simultaneous measurements at alternating heights. Atmosphere 11(10), 1067.

King, J.C., Anderson, P.S., Smith, M.C., Mobbs, S.D., 1996. The surface energy and mass balance at Halley, Antarctica during winter. Journal of Geophysical Researches Atmospheres. 101(D14):19119–19128. https://doi.org/10.1029/96JD01714

Kramm, G., Herbert, F., 2009. Similarity Hypotheses for the Atmospheric Surface Layer Expressed by Non-Dimensional Characteristic Invariants - A Review. The Open Atmospheric Science Journal 3(1), 48–79. https://doi.org10.2174/1874282300903010048

Kułek, B., Weidinger, T., 2023. The Influence of Meteorological Factors and the Time of Day on the Concentration of Ammonia in the Atmosphere Measured Using the Photoacoustic Method near a Cattle Farm—A Case Study. Atmosphere 2023, 14, 1703. https://doi.org/10.3390/atmos14111703

Lettau, H.H., 1979. Wind and Temperature Profile Prediction for Diabatic Surface Layers Including Strong Inversion Cases. Boundary-Layer Meteorology 17(4), 443–464 http://dx.doi.org/10.1007/BF00118610.

Liu, D., Rong, L., Kamp, J., Kong, X., Adamsen, A. P.S., Chowdhury, A., 2020. Photoacoustic measurement with infrared band-pass filters significantly overestimates NH_3 emissions from cattle houses due to volatile organic compound (VOC) interferences. Atmospheric Measurement Techniques 13, 259–272.

Maronga, B., Reuder, J., 2017. On the formulation and universality of Monin-Obukhov similarity functions for mean gradients and standard deviations in the unstable surface layer: results from surface-layer resolving large-eddy simulations, Journal of the Atmospheric Sciences 74, 989–1010 DOI: 10.1175/JAS-D-16-0186.1

Ma, R., Zou, J., Han, Z., Yu, K., Wu, S., Li, Z., Zhu-Barker, X., 2021. Global soil-derived ammonia emissions from agricultural nitrogen fertilizer application: A refinement based on regional and crop-specific emission factors. Global Change Biology 27, 855–867

Mayer, J. C., Bargsten, A., Rummel, U., Meixner, F.X., Foken, T., 2011. Distributed Modified Bowen Ratio method for surface layer fluxes of reactive and non-reactive trace gases. Agricultural and Forest Meteorology, 151(6), 655–668. https://doi.org/10.1016/j.agrformet.2010.10.001.

McVehil, G.E., 1964. Wind and temperature profiles near the ground in stable stratification. Quarterly Journal of the Royal Meteorological Society 90(384), 136–146. https://doi.org/10.1002/qj.49709038403

Miklós, A., Hess, P., Bozóki, Z., 2001. Application of acoustic resonators in photoacoustic trace gas analysis and metrology. Review of scientific instruments 72(4), 1937–1955.

Munro, D.S., Davies, J.A., 1978. On Fitting the Log-linear Model to Wind Speed and Temperature Profiles over a Melting Glacier. - Boundary-Layer Meteorology 15, 423–437.

Nelson, A.J., Lichiheb, N., Koloutsou-Vakakis, S., Rood, M.J., Heuer, M., Myles, L., et al., 2019. Ammonia flux measurements above a corn canopy using relaxed eddy accumulation and a flux gradient system. Agricultural and Forest Meteorology 264, 104–113.

Nemitz, E., Sutton, M.A., Gut, A., San José, R., Husted, S., Schjoerring, J.K., 2000. Sources and sinks of ammonia within an oilseed rape canopy. Agricultural and Forest Meteorology, 105(4), 385-404.

Oren, R.J.S.S., Sperry, J.S., Katul, G.G., Pataki, D.E., Ewers, B.E., Phillips, N., Schäfer, K.V.R., 1999. Survey and synthesis of intra-and interspecific variation in stomatal sensitivity to vapour pressure deficit. Plant, cell & environment 22(12), 1515–1526.

Phillips, S.B., Arya, S.P., Aneja, V.P., 2004. Ammonia flux and dry deposition velocity from near-surface concentration gradient measurements over a grass surface in North Carolina. Atmospheric Environment 38(21), 3469–3480.

Pogány, A., Mohácsi, Á., Jones, S.K., Nemitz, E., Varga, A., Bozóki, Z., ... Szabó, G., 2010. Evaluation of a diode laser based photoacoustic instrument combined with preconcentration sampling for measuring surface–atmosphere exchange of ammonia with the aerodynamic gradient method. Atmospheric Environment, 44(12), 1490–1496.

Rom, H. B., & Zhang, G.Q., 2010. Time delay for aerial ammonia concentration measurements in livestock buildings. Sensors, 10, 4634–4642.

Prueger, J.H., Kustas, W.P., 2005. Aerodynamic Methods for Estimating Turbulent Fluxes. Publications from USDA-ARS / UNL Faculty. 1394. https://digitalcommons.unl.edu/usdaarsfacpub/1394

Seinfeld, J.H., Pandis, S.N., 2016. Atmospheric Chemistry and Physics: From Air Pollution to Climate Change. John Wiley & sons.

Sheppard, P.A., Tribble, D.T., Garratt, J.R., 1972. Studies of turbulence in the surface layer over water (Lough Neagh). Part I. Instrumentation programme, profiles. Quarterly Journal of the Royal Meteorological Society 98, 627–641. https://doi.org/10.1002/qj.49709841711

Shrivastava, A., Gupta, V. B., 2011. Methods for the determination of limit of detection and limit of quantitation of the analytical methods. Chron. Young Sci, 2(1), 21–25.

Sintermann, J., Spirig, C., Jordan, A., Kuhn, U., Ammann, C., Neftel, A., 2011. Eddy covariance flux measurements of ammonia by high temperature chemical ionisation mass spectrometry. Atmospheric Measurement Techniques, 4, 599–616.

Sommer, S.G., Schjoerring, J.K., Denmead, O.T., 2004. Ammonia emission from mineral fertilizers and fertilized crops. In: DL Sparks (ed) Advances in Agronomy 82:557–621.

Spirig, C., Flechard, C.R., Ammann, C., Neftel, A., 2010. The annual ammonia budget of fertilised cut grassland – Part 1: Micrometeorological flux measurements and emissions after slurry application. Biogeosciences 7, 521–536. https://doi.org/10.5194/bg-7-521-2010.

Sutton, M.A., Schjørring, J.K., Wyers, G P., 1995. Plant—atmosphere exchange of ammonia. Philosophical Transactions of the Royal Society of London. Series A: Physical and Engineering Sciences, 351(1696), 261–278.

Sutton, M.A., Reis, S., Riddick, S.N., et al., 2013. Towards a climate-dependent paradigm of ammonia emission and deposition. Philosophical Transactions of the Royal Society B, 368, 20130166. https://doi.org/10.1098/rstb.2013.0166

Swinbank, W.C., 1968. A comparison between prediction of the dimensional analysis for the constant-flux layer and observations in unstable conditions. Quarterly Journal of the Royal Meteorological Society 94, :460–467. https://doi.org/10.1002/qj.49709440203

Toyota, K., Dastoor, A. P., Ryzhkov, A., 2016. Parameterization of gaseous dry deposition in atmospheric chemistry models: Sensitivity to aerodynamic resistance formulations under statically stable conditions. Atmospheric Environment 147, 409–422.

Trebs, I., Ammann, C., Junk, J., 2021. Immission and Dry Deposition. In: Foken, T. (eds) Springer Handbook of Atmospheric Measurements. Springer Handbooks. Springer, Cham. https://doi.org/10.1007/978-3-030-52171-4_54.

Tschalikov, D.V., 1968. O profilja vetra i temperatury v prizemnom sloe atmosfery pri ustojtschivoj stratifikacii (About the wind and temperature profile in the surface layer for stable stratification). Trudy GGO.

von Bobrutzki, K., Braban, C.F., Famulari, D., et al., 2010. Field inter-comparison of eleven atmospheric ammonia measurement techniques. Atmospheric Measurement Techniques, 3, 91–112.

Webb, E.K., 1970. Profile Relationships: the log-linear range, and extension to strong stability. Quarterly Journal of the Royal Meteorological Society 96, 67–90. https://doi.org/10.1002/qj.49709640708

Weidinger, T., Pinto, J., Horváth, L., 2000. Effects of uncertainties in universal functions, roughness length, and displacement height on the calculation of surface layer fluxes. Meteorologische Zeitschrift, 9(3), 139–154. DOI: 10.1127/metz/9/2000/139

Wyer, K.E., Kelleghan, D.B., Blanes-Vidal, V., Schauberger, G., Curran, T. P., 2022. Ammonia emissions from agriculture and their contribution to fine particulate matter: A review of implications for human health. Journal of environmental management 323, 116285. https://doi.org/10.1016/j.jenvman.2022.116285

Xie, Y., Wang, W., Chen, Y., Qian, Z., Chen, J., Tong, J., Li, L., Yue, Y., Chen, K., Chu, Z., Hu, X., 2024. NH_3 emissions and lifetime estimated by satellite observations with a differential evolution algorithm. Atmosphere 15(3), 251. https://doi.org/10.3390/atmos15030251

Xu, R., Tian, H., Pan, S., Prior, S. A., Feng, Y., Batchelor, W.D., et al., 2019. Global ammonia emissions from synthetic nitrogen fertilizer applications in agricultural systems: Empirical and process-based estimates and uncertainty. Global change biology, 25(1), 314–326.

Zahn, E., Bou-Zeid, E., Dias, N.L., 2023. Relaxed eddy accumulation outperforms Monin-Obukhov flux models under non-Ideal conditions. Geophysical Research Letters, 50, e2023GL103099. https://doi.org/10.1029/2023GL103099

Zhan, X., Adalibieke, W., Cui, X., Winiwarter, W., Reis, S., Zhang, L., et al., 2020. Improved estimates of ammonia emissions from global croplands. Environmental Science & Technology 55(2) 1329–1338.

Zilitinkevich, S.S., Tschalikov D.V. 1968. Determining the Universal Wind-Velocity and Temperature Profiles in the Atmospheric Boundary Layer. - Izvestia Atmospheric and Oceanic Physics 4, 294-302 (English version 165–170).

Appendix

Table A1. Universal functions for sensible heat flux in stable stratification for ($0 \le \zeta \le +1$) extended interval.

Reference	Karman constant	Universal function for the exchange of sensible heat
McVehil, (1964)	0.4	$\varphi_H(\zeta) = 1 + 6.3\,\zeta$
Tschalikov, (1968)	0.4	$\varphi_H(\zeta) = 1 + 5.17\,\zeta$
Zilitinkevich and Tschalikov, (1968)	0.43	$\varphi_H(\zeta) = 1 + 9.9\,\zeta, (\zeta \le 0.4), \varphi_H(\zeta) = 4.96, (\zeta > 0.4)$
Zilitinkevich and Tschalikov, (1968)*	0.4	$\varphi_H(\zeta) = 0.95 + 8.9\,\zeta, (\zeta \le 0.4), \varphi_H(\zeta) = 4.51, (\zeta > 0.4)$
Arya and Plate (1969)	0.4	$\varphi_H(\zeta) = 1 + 17.0\,\zeta$
Webb (1970)	0.41	$\varphi_H(\zeta) = 1 + 5.2\,\zeta$
Businger et al. (1971)	0.35	$\varphi_H(\zeta) = 0.74 + 4.7\,\zeta$
Businger et al. (1971)*	0.4	$\varphi_H(\zeta) = 0.95 + 7.8\,\zeta$
Badgley et al. (1972)	0.4	$\varphi_H(\zeta) = 1 + 7\,\zeta$
Sheppard et al. (1972)	0.41	$\varphi_H(\zeta) = 1 + 5.7\,\zeta$
Carl et al. (1973)	0.4	$\varphi_H(\zeta) = 0.74 + 0.963\,\zeta + 29.6\,\zeta^2$ $(\zeta \le 0.08), \varphi_H(\zeta) = 1.2 + 6.1\zeta\ (\zeta > 0.08)$
Dyer (1974)	0.41	$\varphi_H(\zeta) = 1 + 5\,\zeta$
Dyer (1974)*	0.4	$\varphi_H(\zeta) = 0.95 + 4.5\,\zeta$
Munro and Davies (1978)	0.41	$\varphi_H(\zeta) = 1 + 4.3\,\zeta$
Lettau (1979)	0.36	$\varphi_H(\zeta) = 1 + 6.3\,\zeta^{\frac{3}{2}}$
Gavrilov and Petrov (1981)	0.4	$\varphi_H(\zeta) = 0.9 + 6\,\zeta$
Foken and Skeib (1983)	0.4	$\varphi_H(\zeta) = 1\ (\zeta \le 0.125), \varphi_H(\zeta) = \left(\frac{\zeta}{0.125}\right)^2 (\zeta > 0.125)$
Foken and Skeib (1983)*	0.4	$\varphi_H(\zeta) = 0.95\ \ (\zeta \le 0.125), \varphi_H(\zeta) = 0.95\left(\frac{\zeta}{0.125}\right)^2 (\zeta > 0.125)$
Fukui et al. (1983)	0.4	$\varphi_H(\zeta) = 1 + 4.7\,\zeta$
Hurtalova and Szabo (1985)	0.4	$\varphi_H(\zeta) = 1.0 + \zeta(0.118 + 0.405\zeta)^{-1}$ $(\zeta < 0.5), \varphi_H(\zeta) = 2.56\,\zeta \ge 0.5)$
Högström (1988)	0.4	$\varphi_H(\zeta) = 0.95 + 8\,\zeta$
Beljaars and Holtslag (1991)	0.4	$\varphi_H(\zeta) = 1 + \zeta(1 + a\zeta)^b + a\zeta(c - d\eta)e^{-d\zeta}$ where $a = 2/3, b = 1/2, c = 6, d = 0.35$
King et al. (1996)	0.4	$\varphi_H(\zeta) = 0.95\ + 4.99\,\zeta$
Handorf et al. (1999)	0.4	$\varphi_H(\zeta) = 1 + 5\zeta\ (\zeta \le 0.6),\ \varphi_H(\zeta) = 4\ \ (\zeta > 0.6)$
Weidinger et al. (2000)	0.4	$\varphi_H(\zeta) = 1 + 7.5\,\zeta$
Chenge and Brutseart (2005)	0.4	$\varphi_H(\zeta) = 1 + c\frac{\zeta + \zeta^d(1+\zeta^d)^{\frac{1-d}{d}}}{\zeta + (1+\zeta^d)^{\frac{1}{d}}}$, where $c = 5.3, d = 1.1$
Chenge and Brutseart (2005)	0.4	$\varphi_H(\zeta) = 1 + 54\zeta,\ (\zeta \le 0.8), \varphi_H(\zeta) = 5.32, (\zeta > 0.8)$
Edwards et al. (2005)	0.4	$\varphi_H(\zeta) = 1 + 4.7\,\zeta$

*recalculated by Högström (1988) after Foken (2017)

Table A2. Universal functions for sensible heat flux in unstable stratification for ($-1 \le \zeta \le 0$) extended interval.

Reference	**Karman constant**	**Universal function for the exchange of sensible heat**
Swinbank (1968)	0.4	$\varphi_H(\zeta) = 1 + 3.478\,\zeta\ (\zeta \ge -0.1)$ (only extrapolation), $\varphi_H(\zeta) = 0.227(-\zeta)^{-0.44}\ (\zeta < -0.1)$
Zilitinkevich and Chalikov, (1968)	0.434	$\varphi_H(\zeta) = 1 + 1.45\,\zeta,\ (\zeta \ge -0.15),$ $\varphi_H(\zeta) = 0.417\,(-\zeta)^{-\frac{1}{3}}\ (\zeta < -0.15)$
Zilitinkevich and Chalikov, (1968)*	0.4	$\varphi_H(\zeta) = 0.95 + 1.31\,\zeta\ (\zeta \ge -0.15),$ $\varphi_H(\zeta) = 0.4\,(-\zeta)^{-\frac{1}{3}}\ (\zeta < -0.15)$
Dyer and Hicks (1970), Dyer (1974)	0.41	$\varphi_H(\zeta) = (1 - 16\,\zeta)^{-\frac{1}{2}}$
Dyer and Hicks (1970), Dyer (1974)*	0.4	$\varphi_H(\zeta) = 0.95\,(1 - 15.2\,\zeta)^{-\frac{1}{2}}$
Businger et al. (1971)	0.35	$\varphi_H(\zeta) = 0.74\,(1 - 9\,\zeta)^{-\frac{1}{2}}$
Businger et al. (1971)*	0.4	$\varphi_H(\zeta) = 0.95\,(1 - 11.6\,\zeta)^{-\frac{1}{2}}$
Carl et al (1973)	0.4	$\varphi_H(\zeta) = 0.74\,(1 - 16\,\zeta)^{-\frac{1}{2}}$
Lettau (1979)	0.36	$\varphi_H(\zeta) = (1 - 22.5\,\zeta)^{-\frac{1}{2}}$
Dyer and Bradley (1982)	0.4	$\varphi_H(\zeta) = (1 - 14\,\zeta)^{-\frac{1}{2}}$
Foken and Skeib (1983)	0.4	$\varphi_H(\zeta) = 1\ (\zeta \ge -0.06),$ $\varphi_H(\zeta) = (-\frac{\zeta}{0.06})^{-\frac{1}{2}}\ (\zeta < -0.06)$
Foken and Skeib (1983)*	0.4	$\varphi_H(\zeta) = 0.95\ (\zeta \ge -0.06),$ $\varphi_H(\zeta) = 0{,}95(-\frac{\zeta}{0.06})^{-\frac{1}{2}}\ (\zeta < -0.06)$
Fukui et al. (1983)	0.4	$\varphi_H(\zeta) = (1 - 8.5\,\zeta)^{-0.}$
Gavrilov and Petrov (1981)	0.4	$\varphi_H(\zeta) = 0.65\left[(1 - 35\,\zeta)^{-\frac{1}{2}} + \frac{0.25}{1 + 8\,\zeta^2}\right]$
Högström (1988)	0.4	$\varphi_H(\zeta) = 0.95\,(1 - 11.6\,\zeta)^{-\frac{1}{2}}$
Weidinger et al. (2000)	0.4	$\varphi_H(\zeta) = (1 - 12.5\,\zeta)^{-\frac{1}{2}}$
Edwards et al. (2005)	0.4	$\varphi_H(\zeta) = (1 - 15\,\zeta)^{-\frac{1}{2}}$
Maronga and Reuder (2017)	0.4	$\varphi_H(\zeta) = 1.1(1.5 - 17\,\zeta)^{-0.57}$
Maronga and Reuder (2017)	0.4	$\varphi_H(\zeta) = 1.1\,(1.5 - 14.5\,\zeta)^{-0.57}$

*recalculated by Högström (1988) after Foken (2017)

Table A3. Logarithmical profile function for all stability classes with widely used turbulent Prandtl (Pr) numbers.

Pr number	Karman constant	Universal function for the exchange of sensible heat
0.74	0.4	$\varphi_H(\zeta) = 0.74$
1	0.4	$\varphi_H(\zeta) = 1$